

Lattice Thermal Conductivity of the Binary and Ternary Group-IV Alloys Si-Sn, Ge-Sn, and Si-Ge-Sn

S. N. Khatami and Z. Aksamija*

Department of Electrical and Computer Engineering, University of Massachusetts–Amherst, Amherst, Massachusetts 01003-9292, USA

(Received 12 January 2016; revised manuscript received 20 May 2016; published 25 July 2016)

Efficient thermoelectric (TE) energy conversion requires materials with low thermal conductivity and good electronic properties. Si-Ge alloys, and their nanostructures such as thin films and nanowires, have been extensively studied for TE applications; other group-IV alloys, including those containing Sn, have not been given as much attention as TEs, despite their increasing applications in other areas including optoelectronics. We study the lattice thermal conductivity of binary (Si-Sn and Ge-Sn) and ternary (Si-Ge-Sn) alloys and their thin films in the Boltzmann transport formalisms, including a full phonon dispersion and momentum-dependent boundary-roughness scattering. We show that Si-Sn alloys have the lowest conductivity (3 W/mK) of all the bulk alloys, more than 2 times lower than Si-Ge, attributed to the larger difference in mass between the two constituents. In addition, we demonstrate that thin films offer an additional reduction in thermal conductivity, reaching around 1 W/mK in 20-nm-thick Si-Sn, Ge-Sn, and ternary Si-Ge-Sn films, which is near the conductivity of amorphous SiO₂. We conclude that group-IV alloys containing Sn have the potential for high-efficiency TE energy conversion.

DOI: 10.1103/PhysRevApplied.6.014015

I. INTRODUCTION

The current high demand for sustainable and renewable energy sources has instigated tremendous research into alternative sources of energy. Thermoelectric devices, based on the coupling processes between heat and charge transport in many materials, have an increasing potential for practical application in solid-state refrigeration and power generation [1]. Today, high-efficiency thermoelectric conversion devices are used to recover waste heat that is dissipated in industrial processes, engines, and tandem solar cells [2]. The figure of merit which strongly governs thermoelectric efficiency is defined by the dimensionless expression [3]

$$ZT = \frac{S^2 \sigma T}{\kappa_l + \kappa_e}, \quad (1)$$

where S is the Seebeck coefficient, σ is the electrical conductivity, T is the absolute temperature, and κ is the total thermal conductivity including both the carrier and phonon counterparts. Typically, the lattice (phonon) contribution dominates over the electronic counterpart, which means that heat conduction in semiconductors is dominated by phonon transport [4]. Hence, our goal is to optimize ZT by reducing the lattice part of the denominator without having a negative effect on the power factor $S^2 \sigma$, which is then expected to result in higher thermoelectric efficiency.

Silicon is considered to be the basis of modern electronics, which makes it a relatively inexpensive and

abundant semiconductor, especially by comparison to certain other popular room-temperature thermoelectric (TE) materials that have low thermal conductivity, such as bismuth telluride (Bi₂Te₃) [5]. In contrast, Si, as a bulk material, is not a very efficient thermoelectric due to its low conversion efficiency [6], which is limited primarily by a large lattice contribution to the thermal conductivity of 146 W/mK [7,8] at room temperature, and therefore limits the ZT to approximately 0.05 [9]. Similar arguments apply to other bulk group-IV materials including Ge and Sn.

The interdependence of material properties in bulk limits our ability to increase ZT . Hence, approaches have been developed in order to further improve ZT . Alloying and nanostructuring play critical roles in the reduction of thermal conductivity, which results in further increases of ZT over what can be achieved with bulk materials. Alloying two or more bulk materials is among the standard approaches to improve thermoelectric conversion efficiency. The reduction of thermal conductivity is observed in alloying and is used in Si-Ge alloys to achieve $ZT > 1$ at high temperatures (approximately 900 K) [10]. Random mass variation in the alloy results in a significant increase in phonon scattering and a corresponding reduction in thermal conductivity.

However, the thermal conductivity of Si_{1-x}Ge_x reaches a broad plateau in the composition range of 0.2 < x < 0.8 [11], which limits the degree of reduction in lattice thermal conductivity possible in Si-Ge alloys. Within this plateau, changing the thickness has a much greater effect on thermal conductivity than does the variation in Ge composition, while outside of the plateau, compositional variation

*zlatana@engin.umass.edu

dominates. The low-dimensional approach that was proposed by Hicks and Dresselhaus [12,13] is used widely to improve TE conversion efficiency by reducing lattice thermal conductivity. As a result of numerous studies on $\text{Si}_{1-x}\text{Ge}_x$ alloy nanostructures, thermal conductivity 3–5 times lower than the bulk form has been obtained [1]. The reduction of thermal conductivity with respect to the bulk is attributed to the enhancement of boundary scattering [4].

While $\text{Si}_{1-x}\text{Ge}_x$ alloys [14] and their nanostructures (including thin films [15], nanowires [16–18], superlattices [6,19–21], and nanocomposites [22–24]) have been studied widely for TE applications in the past two decades, other group-IV alloys have been given less consideration for TE conversion. Recent interest in Sn-based group-IV alloys is sparked largely by its widely tunable band gap [25], which has opened the possibility to reach direct band gaps [26,27] with potential application in optoelectronics [28,29]. Ternary group-IV alloys $\text{Si}_{1-x-y}\text{Ge}_x\text{Sn}_y$ and their heterostructures are also the subject of research as candidates for IR devices and quantum-well photodiodes [30]. However, the growth of Si-Sn alloys (and to a lesser extent Ge-Sn) with a high Sn concentration remains challenging due to the large lattice mismatch (19.5% between Si and α -Sn) and the low solubility of Sn in Si (approximately $5 \times 10^{19} \text{ cm}^{-3}$) [31].

In this paper, we study binary and ternary alloys of silicon, germanium, and tin in order to determine the lowest possible thermal conductivity achievable in these diamond-structure group-IV alloys. We focus on $\text{Si}_{1-x-y}\text{Ge}_x\text{Sn}_y$ alloys as the underlying material and demonstrate ways of utilizing nanostructuring to reduce the lattice contribution to thermal conductivity, with the ultimate goal of improving the TE figure of merit. Our model is based on solving the phonon Boltzmann transport equation in the relaxation time approximation, including all the relevant intrinsic (three-phonon anharmonic umklapp and normal, isotope, impurity, and alloy mass difference) and extrinsic (due to boundary roughness) scattering mechanisms. We use the full phonon dispersion calculated from the adiabatic bond charge model, and we describe roughness scattering at the boundaries of the nanostructures through a momentum-dependent specular parameter. This paper is organized as follows: The computational model is presented in Sec. II, and Sec. III presents our results on binary and ternary bulk group-IV alloys and their thin films, while Sec. IV summarizes our findings.

II. LATTICE THERMAL CONDUCTIVITY IN BULK ALLOYS AND THIN FILMS

Most theories of transport in solids employ the Boltzmann transport equation (BTE). The distribution function of phonons under a temperature gradient can be obtained by solving the BTE and subsequently used to determine the lattice contribution to thermal conductivity. The steady-state distribution function can be obtained by

solving the time-independent phonon Boltzmann transport equation (PBTE) in the relaxation time approximation, which is well justified in cases where elastic scattering is dominant, such as in our case of alloys and their nanostructures. In the steady state, the time-independent PBTE is given by [32]

$$\vec{v}_{b,\vec{q}} \cdot \vec{\nabla} N_{b,\vec{q}}(x, y, z) = -\frac{N_{b,\vec{q}}(x, y, z) - N_{b,\vec{q}}^0(T)}{\tau_b^{\text{int}}(\vec{q})}. \quad (2)$$

As indicated in the PBTE, the steady-state phonon distribution function $N_{b,q}(x, y, z)$ is a function of the phonon branch b , wave vector q , and position in 3D space (x, y, z) . τ_q^{int} is the relaxation time due to all the intrinsic scattering mechanisms including both resistive umklapp and non-resistive normal anharmonic phonon-phonon, isotope, impurity, and alloy mass difference interactions. τ_q^{int} can be obtained using the standard single-mode relaxation time approximation [33]. The equations hold for each branch, and interbranch scattering is included in $\tau_b^{\text{int}}(\vec{q})$. In the calculation of relaxation time $\tau_b^{\text{int}}(\vec{q})$ for a phonon in mode b and with wave vector \vec{q} , we consider normal $\tau_{b,n}(\vec{q})$ and umklapp $\tau_{b,u}(\vec{q})$ three-phonon scattering, impurity $\tau_{b,I}(\vec{q})$, and mass-disorder $\tau_{b,\text{mass}}(\vec{q})$ scattering. The total intrinsic relaxation time is given by

$$\frac{1}{\tau_b^{\text{int}}(\vec{q})} = \frac{1}{\tau_{b,n}(q)} + \frac{1}{\tau_{b,u}(q)} + \frac{1}{\tau_{b,I}(q)} + \frac{1}{\tau_{b,\text{mass}}(q)}. \quad (3)$$

$\text{Si}_{1-x-y}\text{Ge}_x\text{Sn}_y$ with three materials combined results in a variation in the local atomic mass that leads to a strong mass-difference scattering of phonons. In alloys, mass disorder has three components: alloying, isotopic mass variation, and the small local strain field induced by variations in the atomic species (Si, Ge, or Sn). The scattering strength is proportional to the total of mass-disordered constituents [32]:

$$\Gamma_{\text{mass}}(x) = \Gamma_{\text{alloy}}(x) + \Gamma_{\text{iso}}(x) + \Gamma_{\text{strain}}(x). \quad (4)$$

The alloy mass-difference constant is defined as [34]

$$\Gamma_{\text{alloy}} = \sum_i f_i (1 - M_i/\bar{M})^2, \quad (5)$$

where f_i is the proportion of material i with mass M_i , while the average mass is $\bar{M} = \sum_i f_i M_i$ [33]. Thermal conductivity in the alloys is dramatically reduced by the scattering of phonons from the mass difference between the constituent atoms. The strength of the alloy mass-difference scattering has a quadratic dependence on the ratio between the masses of constituent atoms (M_i) and the average alloy mass (\bar{M}) in Eq. (5).

The energy dependence of the alloy-scattering rate follows a Rayleigh-like ($\tau^{-1} \propto \omega^4$) trend and is calculated from the vibrational density of states as [35,36]

$$\tau_{\text{mass}}^{-1}(\omega) = \frac{\pi}{6} V_0 \Gamma_{\text{mass}} \omega^2 D(\omega), \quad (6)$$

where V_0 is the volume per atom and $D(\omega)$ is the vibrational density of states per unit volume [14]. The total energy-dependent vibrational density of states is given by a sum over all phonon branches b :

$$\begin{aligned} D(\omega) &= \sum_b \int \frac{d\vec{q}}{(2\pi)^3} \delta[\omega - \omega_b(\vec{q})] \\ &= \frac{1}{(2\pi)^3} \sum_{b,i} \frac{S(\omega, \vec{q}_i)}{|\nabla_{\vec{q}} \omega_b(\vec{q}_i)|}. \end{aligned} \quad (7)$$

The volume integral of the energy-conserving delta function over the whole first Brillouin zone (FBZ) is calculated from the full phonon dispersion using the method of Gilat and Raubenheimer [37]. At a given vibrational frequency ω , the Gilat-Raubenheimer method is used to compute the size of the intersection between the constant energy surface, defined as the continuous surface containing all the points in the FBZ such that their dispersion equals a given frequency ω , and the i th discretization cube centered at \vec{q}_i . Finally, the intersection surface area $S(\omega, \vec{q}_i)$ is divided by the norm of the gradient of the dispersion and summed across all the discretization cubes indexed by i to obtain the density of states at a given frequency. Formulas for the constant energy surface area $S(\omega, \vec{q}_i)$ are given in Ref. [37].

The contribution due to the isotopic variation in each of the constituent materials can be obtained by combining the isotope constants for each pure material as

$$\Gamma_{\text{iso}}(x, y) = \frac{(1-x-y)\Gamma_{\text{Si}}M_{\text{Si}}^2 + x\Gamma_{\text{Ge}}M_{\text{Ge}}^2 + y\Gamma_{\text{Sn}}M_{\text{Sn}}^2}{[xM_{\text{Ge}} + (1-x-y)M_{\text{Si}} + yM_{\text{Sn}}]^2}, \quad (8)$$

where the pure silicon and germanium isotope-scattering constants Γ_{Si} and Γ_{Ge} are taken from Ref. [33]. The tin isotope-scattering constant Γ_{Sn} is calculated from the known isotope composition of naturally occurring tin to be $\Gamma_{\text{Sn}} = 3.64 \times 10^{-4}$ based on a similar expression to Eq. (5) which holds for isotope scattering within each material in the alloy [38]. An additional component to alloy scattering arising from the strain field due to the difference in lattice constants of pure Si and Ge and their alloys is proposed. The contribution due to strain is then given by [34]

$$\Gamma_{\text{strain}} = \epsilon \sum_i f_i (1 - a_i/\bar{a})^2, \quad (9)$$

where f_i is the proportion of material i with lattice constant a_i (in this case Si, Ge, and Sn), while the average lattice is given by $\bar{a} = \sum_i f_i a_i$. Here $a_{\text{Si-Ge-Sn}}(x)$ is the composition-dependent alloy lattice constant, taken in the virtual crystal approximation (VCA), including bowing [39]. The empirical strain parameter is taken to be $\epsilon = 39$ [40]. For most values of germanium concentration x , the strain contribution $\Gamma_{\text{strain}}(x)$ is found to be much smaller than the mass-difference component Γ_{alloy} .

The resistive umklapp phonon-phonon scattering rate is calculated in the standard general approximation for dielectric crystals [33]:

$$\tau_{b,u}^{-1}(\vec{q}) = \frac{\hbar \gamma_b^2}{\bar{M} \Theta_b \bar{v}_b^2} \omega_b^2(\vec{q}) T e^{-\Theta_b/3T}, \quad (10)$$

where the speed of sound \bar{v}_b of each branch b is determined from the average slope of its dispersion curve near the Γ point and \bar{M} is the average atomic mass. The Grüneisen parameter γ_b is obtained for each branch from the phonon dispersion and has the value of 1.1 for the longitudinal acoustic branch and -0.6 for the transverse acoustic branches. The expression in Eq. (10) contains the exponential term $e^{-\Theta_b/3T}$ in the temperature dependence, which controls the onset of resistive umklapp scattering for each phonon branch through the branch-specific Debye temperatures Θ_λ , which are obtained from Ref. [41]:

$$\Theta_b^2 = \frac{5\hbar^2 \int \omega^2 g_b(\omega) d\omega}{3k_B^2 \int g_b(\omega) d\omega}, \quad (11)$$

where the vibrational density of states function $g_b(\omega) = \sum_{\vec{q}} \delta[\omega - \omega_b(\vec{q})]$ is calculated for each phonon branch b from the full dispersion. This way, the temperature dependence of the contribution from each phonon branch to the total thermal conductivity is correctly represented.

In the bulk case, the crystal is assumed infinite and uniform. The distribution is only a function of temperature, and, in the absence of boundaries and interfaces, the solution of the PBTE is simply given by

$$n_{\vec{q}} = \tau_{\text{int}}(\vec{q}) \bar{v}_{\vec{q}} \cdot \nabla_{\vec{r}} T \frac{\partial N_{\vec{q}}^0(T)}{\partial T}. \quad (12)$$

In contrast, boundaries and interfaces play an important role in the solution of the PBTE in nanostructures. Hence, in nanostructures, we have to add an extrinsic relaxation rate $\tau_{b,B}^{-1}(\vec{q})$ due to boundary-roughness (B) scattering. Each time a phonon reaches the boundary, we capture the probability of it not being scattered by the roughness through the momentum-dependent specularly parameter $0 < p(\vec{q}) < 1$ given by

$$p(\vec{q}) = \exp(-4\Delta^2 q^2 \cos^2 \Theta) \quad (13)$$

with Δ being the rms boundary roughness (typically $0.1 < \Delta < 1$ nm, depending on the sample quality and processing) and Θ being the angle between the direction of propagation of the phonon wave and the boundary normal. The specularity parameter allows us to capture both the magnitude and angle dependence of the boundary scattering and distinguish between the contribution to the heat flux from phonons traveling into the boundary [small Θ and, hence, smaller $p(\vec{q})$ and more scattering] and phonons traveling parallel to the boundary [large Θ and larger $p(\vec{q})$, leading to less scattering].

The specularity parameter is used in solving the PBTE as a boundary condition, with $[1 - p(\vec{q})]$ giving the fraction of the incoming phonons which are scattered randomly. As boundary scattering is a momentum-randomizing elastic process, the scattered phonons will carry zero heat flux, so they can be represented by the equilibrium Bose-Einstein distribution, leading to a boundary condition of the form

$$N_b(\vec{q})^+ = p(\vec{q})N_b(\vec{q})^- + [1 - p(\vec{q})]N_{b,T}^0(\vec{q}), \quad (14)$$

with $+$ and $-$ representing the solution before reaching and after leaving the boundary, respectively, and $N_0(\vec{q})$ is the equilibrium Bose-Einstein phonon distribution of phonon mode \vec{q} in branch b . The boundary-scattering rate for a film of thickness H is then obtained as [6]

$$\tau_{b,B}^{-1}(\vec{q}) = \frac{v_{b,\perp}(\vec{q})}{H} \frac{F_p(\vec{q}, H)}{1 - \frac{\tau_b^{\text{int}}(\vec{q})v_{b,\perp}(\vec{q})}{H} F_p(\vec{q}, H)}, \quad (15)$$

where a mode-dependent scaling factor $F_p(\vec{q}, H)$ is given by

$$F_p(\vec{q}, H) = \frac{[1 - p(\vec{q})]\{1 - \exp[-H/\tau_b^{\text{int}}(\vec{q})v_{b,\perp}(\vec{q})]\}}{1 - p(\vec{q}) \exp[-H/\tau_b^{\text{int}}(\vec{q})v_{b,\perp}(\vec{q})]}. \quad (16)$$

This formulation of interface scattering allows for the rates of internal (intrinsic) and boundary-roughness scattering to be added together, despite their interdependence [42]. The factor given by Eq. (16) encapsulates the competition between the boundary and internal scattering: The effective strength of boundary scattering depends on the relative strength of the competing internal scattering mechanisms [43].

Our approach describes supported thin films with flat, partially diffuse boundaries having uncorrelated atomic-scale roughness [4]; however, it does not take into account the modification of phonon dispersion in ultrathin films, which is found to lower group velocity further in pure suspended Si thin films below approximately 30 nm [44], resulting in reductions of thermal conductivity below those predicted by the diffuse model. Thin films or other nanostructures that are nanoporous [45] or have surface

modification [46] can lead to even further reduction of the thermal conductivity, reaching in some nanocrystalline cases below the so-called amorphous limit [47], which we discuss in more detail in the next section. In contrast, alloy nanostructures such as Si-Ge nanowires [18] are found to have a significantly shorter phonon mean free path (MFP) due to strong alloy scattering, which leads to heat being carried mostly by long-wavelength phonons having a dominant phonon wavelength of around 10 nm; hence, we expect our model to be quantitative in thin films having a thickness down to around 20 nm, as well as a qualitative upper bound on what may be achievable in sub-20-nm films that are further modified by nanoporosity, surface modification, or having a nanocrystalline internal structure.

The full thermal conductivity tensor $\kappa^{\alpha\beta}$ is obtained as a sum over all phonon momenta and branches [48]:

$$\kappa^{\alpha\beta} = \sum_{b,\vec{q}} \tau_b(\vec{q}) C_{b,T}(\vec{q}) v_b^\alpha(\vec{q}) v_b^\beta(\vec{q}), \quad (17)$$

where $\tau_b(\vec{q})$ is the total phonon relaxation time [for a bulk sample, $\tau_b(\vec{q}) = \tau_{b,\text{internal}}(\vec{q})$ from Eq. (3)] and the phonon heat capacity per mode $C_{b,T}(\vec{q})$ is given by

$$C_{b,T}(\vec{q}) = \frac{[\hbar\omega_b(\vec{q})]^2}{k_B T^2} \frac{e^{[\hbar\omega_b(\vec{q})/k_B T]}}{[e^{[\hbar\omega_b(\vec{q})/k_B T]} - 1]^2}, \quad (18)$$

where $v_b^\alpha(\vec{q})$ is a component of the phonon velocity vector calculated from the full phonon dispersion based on Weber's adiabatic bond charge (ABC) model [49]. The ABC model includes interactions between ions, bond charges, bond bending, and long-range electrostatic interactions and has been shown to reproduce measured phonon vibrational frequencies in virtually all group-IV [4,49–51], -III–V [51,52], and -II–VI [53] semiconductors with excellent accuracy. The ABC phonon dispersions for Si can be found in Refs. [4,49] and for Ge in Refs. [49,51]. The vibrational properties of $\text{Si}_{1-x}\text{Ge}_x\text{Sn}_y$ alloys, including phonon dispersion and velocity, are calculated here in the VCA [40]. The VCA is shown to capture the acoustic phonon modes and thermal conductivities of silicon and its alloys [54] as well as $\text{PbTe}_{1-x}\text{Se}_x$ alloys [55] with good accuracy.

We calculate the dispersion of each bulk alloy at a dense grid of 64 000 points throughout the whole FBZ. We also compute phonon group velocities from the gradient of dispersion $\vec{v}_b(\vec{q}) = d\omega_b/d\vec{q}$ using the finite difference and store the three components (x , y , and z) of group velocity at each discretization point. The calculated phonon dispersion of pure α -Sn (solid curve), as well as binary alloys $\text{Ge}_{0.5}\text{Sn}_{0.5}$ (dotted curve) and $\text{Si}_{0.5}\text{Sn}_{0.5}$ (dashed curve) along the crystallographic symmetry directions, is shown in Fig. 1. The experimental data taken from soft neutron-scattering measurements reported in Ref. [56] match with the numerical simulation results we obtain. α -Sn with the atomic mass of 118.71 amu has a higher

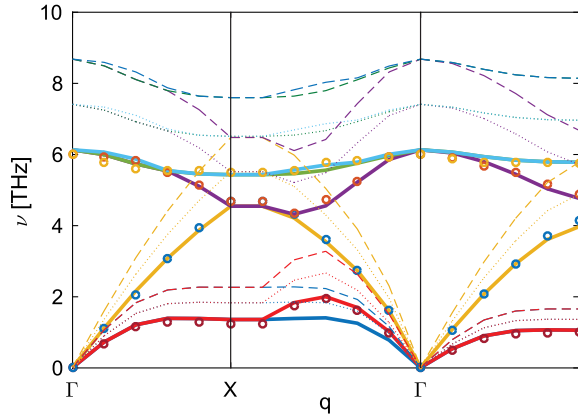


FIG. 1. Phonon dispersion curves [the vibrational frequencies (THz)] for α -Sn, $\text{Ge}_{0.5}\text{Sn}_{0.5}$, and $\text{Si}_{0.5}\text{Sn}_{0.5}$ showing vs the phonon wave vector. The symbols represent the experimental measurement of α -Sn from Ref. [56], and solid lines are the numerical simulation of α -Sn. Dotted lines represent the dispersion of $\text{Ge}_{0.5}\text{Sn}_{0.5}$, and dashed lines depict the dispersion of $\text{Si}_{0.5}\text{Sn}_{0.5}$.

atomic mass and, therefore, a larger density in comparison with silicon and germanium with the atomic mass of 28.0855 and 72.640 amu, respectively. This results in a lower vibrational frequency in the dispersion curves of α -Sn compared to $\text{Ge}_{0.5}\text{Sn}_{0.5}$ and even more so in comparison to $\text{Si}_{0.5}\text{Sn}_{0.5}$, as seen in Fig. 1. The general trend we observe is that a heavier average atomic mass leads to flatter dispersion curves. Consequently, alloys containing Sn have a lower phonon group velocity, and we expect a decrease in the thermal conductivity of Sn-based group-IV alloys.

III. RESULTS

The lattice thermal conductivity of bulk ternary alloy Si-Ge-Sn is calculated from our full-dispersion PBTE model. The top plot in Fig. 2 depicts the thermal conductivity of bulk Si-Ge-Sn alloys against their contributed composition. The thermal conductivity of binary alloys Si-Ge, Si-Sn, and Ge-Sn can also be seen along the edges where germanium, silicon, and tin compositions are equal to zero for Si-Sn, Ge-Sn, and Si-Ge, respectively. We note here the broad plateau that the thermal conductivity reaches in the alloy composition range of $0.2 < x < 0.8$ for germanium composition in $\text{Si}_{1-x}\text{Ge}_x$ and $0.2 < y < 0.8$ for tin composition in $\text{Si}_{1-y}\text{Sn}_y$, and a similar plateau for Ge-Sn; the amount of reduction in the lattice thermal conductivity which can be achieved through alloying alone is somewhat limited.

The reason for this broad plateau is related to the dominant mass-disorder scattering in alloys which depends quadratically on the difference in atomic mass between the constituent materials and the average mass. In this wide middle plateau region, scattering from the alloy mass disorder is strongly dominant over all other intrinsic

mechanisms, including both umklapp and normal phonon-phonon scattering as well as the weak isotopic mass disorder. In addition, our results shown in the bottom plot in Fig. 2 demonstrate that adding the heavier Sn into the alloy results in a further reduction of the thermal conductivity below the minimum value achievable in Si-Ge. The lowest thermal conductivity for bulk binary alloys Si-Sn is 3 W/mK, reached at a Sn composition of 0.5, and 5.86 W/mK in Ge-Sn at a Sn composition of 0.61, in agreement with the range of values (5–9 W/mK) measured in annealed poly-Ge-Sn [57]. These values are significantly lower than the lowest thermal conductivity of bulk Si-Ge, which is 6.67 W/mK at a Ge composition of 0.38. Among these alloys, the binary Si-Sn alloy is found to have the lowest bulk thermal conductivity, in good agreement with reverse non-equilibrium molecular dynamics simulations at the mass ratio of 4.2 between Si and Sn [58]. The reduction is explained by the larger mass difference between Si and Sn which results in a higher mass-disorder scattering rate and, hence, a lower lattice thermal conductivity [59].

Bulk Si-Sn alloys at such a high Sn concentration have not been demonstrated due to the low solid solubility of Sn

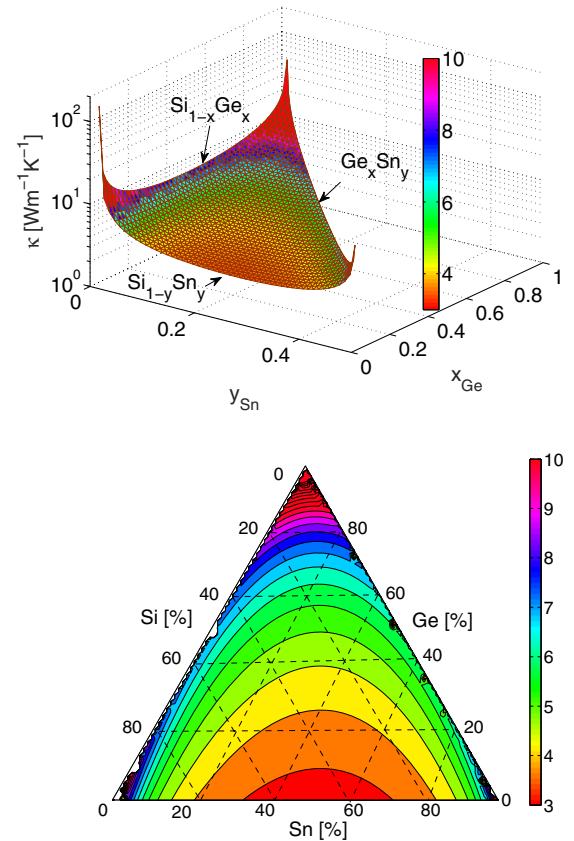


FIG. 2. (Top) A 3D surface plot of thermal conductivity vs Sn and Ge composition for Si-Sn, Ge-Sn, and Si-Ge of bulk material. Si-Sn has the lowest thermal conductivity in the bulk form. (Bottom) A ternary plot of thermal conductivity vs alloy composition.

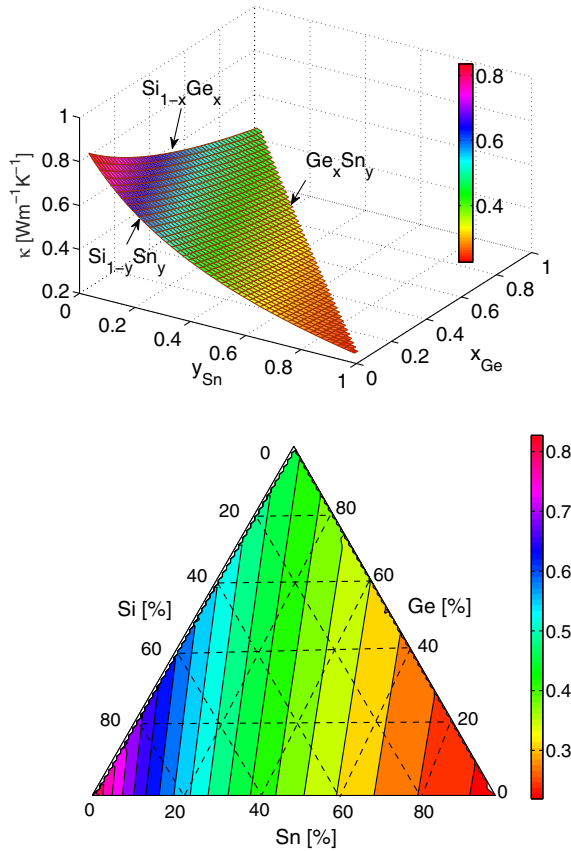


FIG. 3. (Top) A 3D surface plot of the lowest achievable thermal conductivity vs alloy composition for Si-Ge-Sn. Binary alloys correspond to the edges of the triangle of data points, showing that Sn has the lowest thermal conductivity in the amorphous (disordered) limit.

in Si; nonetheless, the thermal conductivity at 18% Sn concentration, the highest Sn fraction demonstrated so far [60], is 3.73 W/mK, which is nearly a 44% reduction from the lowest bulk Si-Ge value. Therefore, we expect this reduction in lattice thermal conductivity to translate to a corresponding 44% increase in the thermoelectric figure of merit ZT . A ZT value of 1 is reported in n -type Si-Ge alloys at approximately 900 °C [61] and subsequently increased to 1.3 through nanostructuring [23]; although there are no reports on the Seebeck coefficient of Si-Sn, the weak dependence of the thermoelectric properties on the alloy composition in Si-Ge leads us to estimate that the reduction in thermal conductivity resulting from the introduction of Sn can lead to a figure of merit ZT of up to 1.35 in bulk alloys at 18% Sn concentration and up to 2.1 if a $\text{Si}_{0.5}\text{Sn}_{0.5}$ alloy could be achieved. However, further investigation on the electronic transport and power factor of group-IV alloys containing Sn, as well as further work on the synthesis of alloys with a large Sn concentration, is needed.

We contrast the bulk-alloy results to their corresponding theoretical minimum values, often called the amorphous limit, which would be achieved in a crystal having maximum disorder while retaining bulk vibrational modes.

This model, while only approximate and not necessarily a general lower bound [47], provides us with some indication of what conductivity might be achievable through disorder (a combination of mass or alloy and boundary roughness) in a crystalline material. In order to calculate the amorphous-limit values of thermal conductivity, we rely on Cahill's minimum thermal conductivity model [62] and calculate the maximum scattering rate directly as one-half period of the vibrational frequency ω/π . The calculated amorphous (disordered) thermal conductivity of ternary alloys of Si-Ge-Sn are shown in the surface (top) and ternary (bottom) plots in Fig. 3. Unlike the bulk results, there is no plateau, and pure Sn has the lowest achievable thermal conductivity in comparison with all other alloy compositions due to its lowest vibrational frequencies of the three materials. We find that the amorphous-limit values are all below 1 W/mK; consequently, there is room to reduce the thermal conductivity further through size effects caused by boundary-roughness scattering in nanostructures. Next, we study the lattice thermal conductivity of alloy thin films in order to further decrease the thermal conductivity towards the amorphous limit. The results of our calculations for thin Si-Ge alloy films are depicted in the top plot in Fig. 4; these results are validated through a

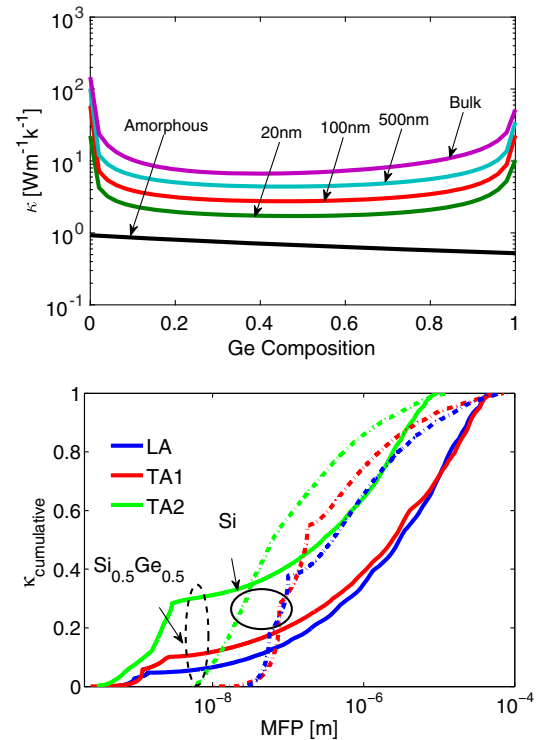


FIG. 4. (Top) Lattice thermal conductivity of binary alloy Si-Ge vs Ge composition for bulk, 500-, 100-, and 20-nm thickness at room temperature. The sample thickness is 1 μm for nanostructures with 0.45-nm roughness. The bottom line shows the lowest achievable thermal conductivity amorphous limit of Si-Ge vs Ge composition. (Bottom) Cumulative thermal conductivity of pure Si (dashed lines) and Si-Ge alloy (solid lines) for acoustic branches.

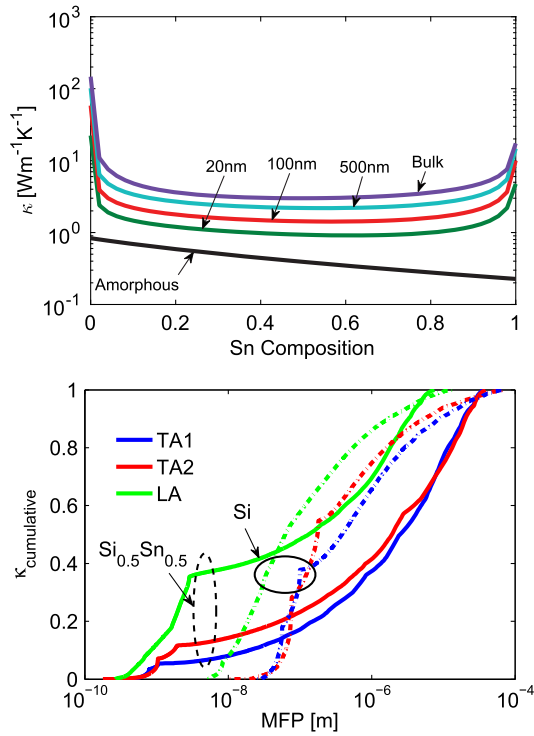


FIG. 5. (Top) Lattice thermal conductivity of binary alloy Si-Sn vs Sn composition for bulk, 500-, 100-, and 20-nm thickness. The simulation is done at room temperature with a roughness of 0.45 nm and a sample thickness of 1 μm for nanostructures. The bottom line depicts the amorphous-limit thermal conductivity of the alloy against Sn composition, while the top line shows the thermal conductivity of bulk Si-Sn. (Bottom) Cumulative thermal conductivity vs mean free path of pure Si (dashed lines) and Si-Sn alloy (solid lines).

comparison with experimental data from Cheaito *et al.* [15] in a previous publication [1]. Overall, the trends follow the expected reduction due to extrinsic boundary scattering in thin films. We include Si-Ge results here mainly for comparison with our results in Figs. 5 and 6 for Si-Sn and Ge-Sn, respectively.

Comparing the results across compositions at a fixed film thickness, we find that the thermal conductivity of Si-Ge thin alloy films reaches the lowest value of 1.71 W/mK at 20-nm thickness for a Ge composition of 0.48. In contrast, the lowest thermal conductivity for Si-Sn at 20-nm thickness is 0.91 W/mK, achieved at a Sn composition of 0.59 Sn. This value is below that of a high-performance thermoelectric Bi-Sb-Te alloy nanocomposite ($\kappa_{ph} = 1.1$ W/mK at room temperature) having a comparable (20-nm average) grain size [63]. Such high Sn compositions exceeding 18% may be achievable only in very thin films; however, we note here that at a 0.18 Sn composition and 20-nm thickness, the thermal conductivity increases only to 1.22 W/mK because of the broad plateau in thermal conductivity vs composition, which can be seen in Fig. 5. This value still represents nearly a 30% reduction

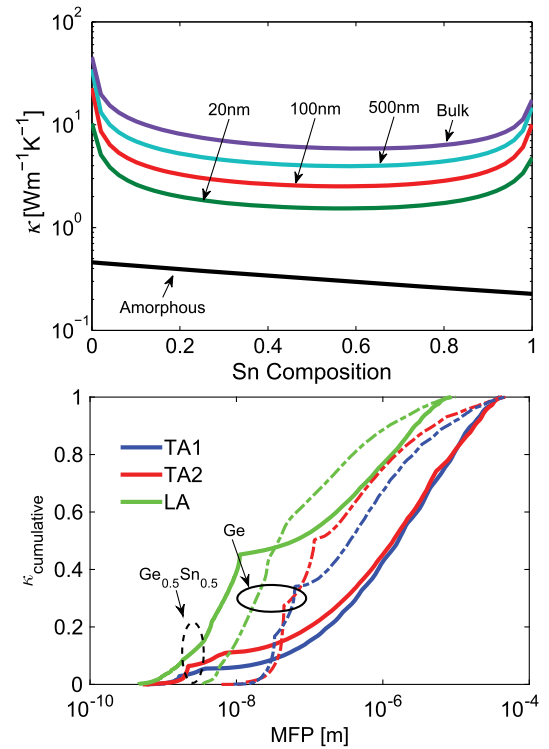


FIG. 6. (Top) Lattice thermal conductivity of binary Ge-Sn vs Sn composition for bulk, 500-, 100-, and 20-nm thickness. The simulation is done at room temperature with a roughness of 0.45 nm and 1- μm in-plane sample length. The bottom line depicts the amorphous-limit thermal conductivity of the alloy against Sn composition, while the top line shows the thermal conductivity of bulk Si-Sn. (Bottom) Cumulative thermal conductivity vs mean free path of pure Si (dashed lines) and Si-Sn alloy (solid lines).

from the lowest value achievable in Si-Ge thin films of equal 20-nm thickness. A room-temperature thermal conductivity of 2.5 W/mK, of which 1.8 W/mK is the lattice contribution due to phonons, is reported in a $\text{Si}_{0.8}\text{Ge}_{0.2}$ nanocomposite having an average nanoparticle size of about 20 nm. This nanocomposite reaches a ZT of about 1.3 at 900 $^{\circ}\text{C}$ [23,64]; our calculated thermal conductivity value is 50% smaller, leading us to estimate the potential ZT that could be reached in a $\text{Si}_{0.82}\text{Sn}_{0.18}$ nanocomposite with the same 20-nm nanoparticle size to be around 1.7, assuming the same electron contribution to thermal conductivity $\kappa_e = 0.7$ W/mK. In p -type Si-Ge nanocomposites, the peak ZT value is around 30% smaller than n -type, likely due to lower hole mobility [65], reaching 0.95 at 850 $^{\circ}\text{C}$ [22,66]. However, recent reports indicate that hole mobility in Si-Sn alloys is 13% higher than in silicon [67]; therefore, we expect that the combination of increased mobility and reduced thermal conductivity could bring p -type Si-Sn alloys closer in line with their n -type counterparts.

In alloy thin films, we plot and analyze the cumulative mean-free-path distributions which are commonly used to

study the impact of size effects on thermal conductivity. The bottom plots in Figs. 4, 5, and 6 show the cumulative thermal conductivity vs mean free path for the pure and alloy bulk of Si-Ge, Si-Sn, and Ge-Sn, respectively. The cumulative thermal conductivity is scaled by the total thermal conductivity so that it shows how lattice thermal conductivity is accumulated against the phonon mean free path, thus allowing us to visualize and compare the extent to which restricting the phonon mean free paths via nanostructuring can result in a thermal conductivity reduction [68]. In the diffuse case, boundary scattering limits the phonon MFP to be smaller than or equal to the thickness of the film; hence, only phonons having a mean free path smaller than or equal to the film thickness will maintain their contribution to the thermal conductivity in the thin film. The resulting thermal conductivity can be seen in the cumulative distribution by taking the MFP equal to the thickness and reading off the corresponding thermal conductivity (the resulting value indicates the fraction of conductivity which persists in the thin film). Because the density of states peaks near van Hove singularities, there are sharp bends in the slope of the cumulative thermal conductivity plot corresponding to these peaks. Throughout these plots, we focus on the longitudinal and transverse acoustic modes and omit the optical ones due to their low contribution to thermal conductivity, caused by their very flat dispersion and consequently low-phonon group velocities.

The bottom plot in Fig. 4 shows the cumulative thermal conductivity against MFP for Si-Ge alloy (solid lines) and pure Si (dashed lines). Phonons with MFPs of $1 \mu\text{m}$ or more contribute around 50% of the thermal conductivity in pure Si; in contrast, phonons with such long MFPs in $\text{Si}_{0.5}\text{Ge}_{0.5}$ alloy have a significantly lower contribution. However, the alloy curves show a broader and more gradual distribution, with a larger contribution from MFPs below 100 nm. Consequently, the range of phonon MFPs which can be used to reduce thermal conductivity extends further into the nanoscale regime, requiring thinner films or wires to reach a substantial reduction. Hence, the combination of alloying and nanostructuring provides a broader range of tunable mean free paths that can be used to reduce the thermal conductivity and ultimately improve the TE efficiency. In Si-Sn (Fig. 5), phonons having MFPs below 20 nm still contribute around 40% of the thermal conductivity, significantly more than they contribute in Si-Ge, thereby leaving more opportunity to further reduce the thermal conductivity and improve the TE figure of merit through a combination of alloying and nanostructuring.

For Ge-Sn thin films, shown in Fig. 6, the lowest thermal conductivity value achieved in a 20-nm thin film is 1.53 W/mK , obtained at a Sn composition of $y = 0.55$. Epitaxial Ge-Sn and ternary Si-Ge-Sn alloy layers on Si are demonstrated and employed in the literature [69,70] with a larger Sn concentration than their Si-Sn counterparts. The

cumulative thermal conductivity against MFP of Ge-Sn (Fig. 6, bottom) follows a trend similar to its Si-Sn counterpart, shown in Fig. 5 (bottom) but with even more conductivity persisting down to 20-nm MFPs; consequently, even in 20-nm thin films, the thermal conductivity in Ge-Sn alloys is well above the corresponding amorphous limit (0.30 W/mK at 0.59 Sn). Ge-Sn alloys are theoretically predicted to have a higher mobility than Si, especially under strain [71]. In addition, relaxed Ge-Sn becomes a direct band-gap semiconductor at Sn concentrations exceeding 7.3%, and the band gap scales towards zero in proportion to the concentration of tin [26]. For thermoelectric applications, the figure of merit ZT typically peaks at a temperature where the band gap is approximately 10 times the thermal energy $E_G = 10k_B T_{\text{peak}}$ [72]. The composition-tunable band gap implies that the ZT peak can be shifted to lower temperatures by increasing the proportion of Sn. Doing so also has the added benefit of obtaining a lower lattice thermal conductivity.

In Fig. 7, we depict the ternary alloy thermal conductivity vs Ge and Sn composition. We keep the germanium and tin compositions, x and y , respectively, equal ($x = y$) and vary them from 0 to 0.5, while the silicon composition

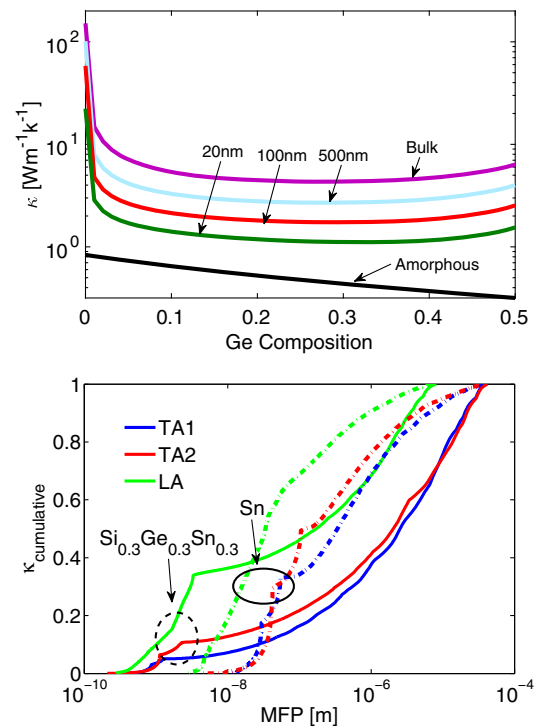


FIG. 7. (Top) Lattice thermal conductivity of ternary alloy Si-Ge-Sn vs Ge or Sn composition for bulk, 500-, 100-, and 20-nm thickness at room temperature with 0.45-nm roughness and $1\text{-}\mu\text{m}$ in-plane film length. The bottom black line shows the lowest achievable thermal conductivity of the alloy against Ge or Sn composition. (Bottom) Cumulative thermal conductivity vs mean free path of pure Sn (dashed lines) and $\text{Si}_{0.3}\text{Ge}_{0.3}\text{Sn}_{0.3}$ alloy (solid lines).

$(1 - x - y)$ is reduced from 1 to 0. At germanium and tin compositions of $x = y = 0.32$ and a film thickness of 20 nm, the thermal conductivity reaches its lowest value of 1.11 W/mK, which is lower than the Si-Ge thermal conductivity at the same thickness but slightly higher than the lowest value achieved in Si-Sn at that same thickness. However, this is the closest value to the lowest achievable thermal conductivity given by the corresponding amorphous limit. Cumulative contributions to thermal conductivity vs phonon mean free path are also depicted in the bottom plot in Fig. 7, which shows that alloying leads to a broader range and a more gradual dependence on mean free paths, allowing us to further decrease the thermal conductivity and possibly improve the TE figure of merit ZT through nanostructuring. Ternary alloys allow the decoupling of the band gap from the lattice constant [30], so that the band-gap value can potentially be reduced while reducing the large lattice mismatch between α -Sn and either Si or Ge.

IV. CONCLUSIONS AND DISCUSSION

We calculate the lattice contribution to thermal conductivity in binary and ternary group-IV alloys by solving the phonon Boltzmann transport equation in the relaxation time approximation. Our model includes phonon scattering with all intrinsic scattering mechanisms (three-phonon umklapp and normal, isotope, impurity, and mass-difference alloy scattering) as well as interactions with partially diffuse boundaries of the nanostructures described by a momentum-dependent model for phonon scattering with boundary roughness. We use the full phonon dispersion computed from the adiabatic bond charge model and combine the phonon dispersions for alloys in the virtual crystal approximation. We find that thermal conductivity is tunable by both thickness and alloying over a wide range of values. A significant reduction in the thermal conductivity in Sn-based alloys is observed in both bulk and thin-film form in comparison with Si-Ge alloys at the same composition and thickness. Si and Sn have the largest mass difference, leading to the highest mass-difference scattering in the Si-Sn alloy of all the binary combinations and, hence, the lowest thermal conductivity. In nanostructures, we find a further reduction in the thermal conductivity due to size effects, to values far below their bulk counterparts and nearly reaching the amorphous limit. The 20-nm-thick films of Si-Sn and Si-Ge-Sn all have conductivities approaching 1 W/mK, which is the thermal conductivity of amorphous SiO_2 .

Our results demonstrate that binary and ternary group-IV alloys involving Sn have a low lattice thermal conductivity and, therefore, may have potential as high-efficiency Si-compatible TE materials, especially in nanostructured form. In addition to the low lattice thermal conductivity well below their Si-Ge counterparts, group-IV alloys containing Sn have tunable band gaps which may expand

the range of temperatures where they are competitive with existing materials. For example, bulk Bi_2Te_3 is commonly used at room temperature because of the combination of its smaller band gap (150 meV at room temperature [73]) and low thermal conductivity (1.4 W/mK measured in a 1- μm film [74]); both of these are achievable with Si-Ge-Sn alloys, alongside being compatible with current Si-based nanoelectronics. While it is too early to fully evaluate the potential for Si-Ge-Sn to replace or improve on existing TE materials, we expect that these findings will spur further research into the growth of bulk and nanostructured group-IV alloys containing Sn and their optimization for TE applications.

The lattice thermal conductivity in the alloys we study shows a broad plateau for alloy concentrations between 0.2 and 0.8; in addition, alloy and boundary-roughness scattering largely suppress the temperature dependence of the lattice thermal conductivity. Hence, we believe our results are applicable to a wide range of compositions and sizes and can be used as a guide in the future design, selection, and further optimization of group-IV alloys and their nanostructures such as multilayers [59] for high- ZT TE applications, with possible ZT values increasing up to 1.7 in $\text{Si}_{0.82}\text{Sn}_{0.18}$ nanocomposites; however, further work on the composition dependence of the thermoelectric power factor is needed to realize these possibilities. In addition, the synthesis of group-IV alloys having a large concentration of Sn remains a challenge. Finally, we believe our results will also inform applications of Si-Ge-Sn alloys in optoelectronics, enabled by the transition from indirect to direct band gap, where thermal dissipation may hamper some applications due to inefficient heat removal through the alloys having a lower thermal conductivity.

-
- [1] M. Mupadhyaya, S. N. Khatami, and Z. Aksamija, Engineering thermal transport in SiGe-based nanostructures for thermoelectric applications, *J. Mater. Res.* **30**, 2649 (2015).
 - [2] B. Lorenzi, M. Acciarri, and D. Narducci, Conditions for beneficial coupling of thermoelectric and photovoltaic devices, *J. Mater. Res.* **30**, 2663 (2015).
 - [3] F. J. DiSalvo, Thermoelectric cooling and power generation, *Science* **285**, 703 (1999).
 - [4] Z. Aksamija and I. Knezevic, Anisotropy and boundary scattering in the lattice thermal conductivity of silicon nanomembranes, *Phys. Rev. B* **82**, 045319 (2010).
 - [5] Z. Aksamija and U. Ravaioli, Anharmonic decay of g-process longitudinal optical phonons in silicon, *Appl. Phys. Lett.* **96**, 091911 (2010).
 - [6] Z. Aksamija and I. Knezevic, Thermal conductivity of $\text{Si}_{1-x}\text{Ge}_x/\text{Si}_{1-y}\text{Ge}_y$ superlattices: Competition between interfacial and internal scattering, *Phys. Rev. B* **88**, 155318 (2013).
 - [7] C. J. Glassbrenner and G. A. Slack, Thermal conductivity of silicon and germanium from 3°K to the melting point, *Phys. Rev.* **134**, A1058 (1964).

- [8] P. D. Maycock, Thermal conductivity of silicon, germanium, III–V compounds and III–V alloys, *Solid State Electron.* **10**, 161 (1967).
- [9] C. N. Liao, C. Chen, and K. N. Tu, Thermoelectric characterization of Si thin films in silicon-on-insulator wafers, *J. Appl. Phys.* **86**, 3204 (1999).
- [10] G. J. Snyder and E. S. Toberer, Complex thermoelectric materials, *Nat. Mater.* **7**, 105 (2008).
- [11] C. Bera, M. Soulier, C. Navone, G. Roux, J. Simon, S. Volz, and N. Mingo, Thermoelectric properties of nanostructured $\text{Si}_{1-x}\text{Ge}_x$ and potential for further improvement, *J. Appl. Phys.* **108**, 124306 (2010).
- [12] L. D. Hicks and M. S. Dresselhaus, Effect of quantum-well structures on the thermoelectric figure of merit, *Phys. Rev. B* **47**, 12727 (1993).
- [13] M. S. Dresselhaus, G. Chen, M. Y. Tang, R. G. Yang, H. Lee, D. Z. Wang, Z. F. Ren, J.-P. Fleurial, and P. Gogna, New directions for low-dimensional thermoelectric materials, *Adv. Mater.* **19**, 1043 (2007).
- [14] J. Garg, N. Bonini, B. Kozinsky, and N. Marzari, Role of Disorder and Anharmonicity in the Thermal Conductivity of Silicon-Germanium Alloys: A First-Principles Study, *Phys. Rev. Lett.* **106**, 045901 (2011).
- [15] R. Cheaito, J. C. Duda, T. E. Beechem, K. Hattar, J. F. Ihlefeld, D. L. Medlin, M. A. Rodriguez, M. J. Champion, E. S. Piekos, and P. E. Hopkins, Experimental Investigation of Size Effects on the Thermal Conductivity of Silicon-Germanium Alloy Thin Films, *Phys. Rev. Lett.* **109**, 195901 (2012).
- [16] Z. Wang and N. Mingo, Diameter dependence of SiGe nanowire thermal conductivity, *Appl. Phys. Lett.* **97**, 101903 (2010).
- [17] Eun Kyung Lee *et al.*, Large thermoelectric figure-of-merits from SiGe nanowires by simultaneously measuring electrical and thermal transport properties, *Nano Lett.* **12**, 2918 (2012).
- [18] T. K. Hsiao, H. K. Chang, S. C. Liou, M. W. Chu, S. C. Lee, and C. W. Chang, Observation of room-temperature ballistic thermal conduction persisting over $8.3 \mu\text{m}$ in SiGe nanowires, *Nat. Nanotechnol.* **8**, 534 (2013).
- [19] S.-M. Lee, D. G. Cahill, and R. Venkatasubramanian, Thermal conductivity of Si-Ge superlattices, *Appl. Phys. Lett.* **70**, 2957 (1997).
- [20] M. L. Lee and R. Venkatasubramanian, Effect of nanodot areal density and period on thermal conductivity in SiGe/Si nanodot superlattices, *Appl. Phys. Lett.* **92**, 053112 (2008).
- [21] W. L. Liu, T. Borca-Tasciuc, G. Chen, J. L. Liu, and K. L. Wang, Anisotropic thermal conductivity of Ge quantum-dot and symmetrically strained Si/Ge superlattices, *J. Nanosci. Nanotechnol.* **1**, 39 (2001).
- [22] Giri Joshi *et al.*, Enhanced thermoelectric figure-of-merit in nanostructured p-type silicon germanium bulk alloys, *Nano Lett.* **8**, 4670 (2008).
- [23] X. W. Wang *et al.*, Enhanced thermoelectric figure of merit in nanostructured n-type silicon germanium bulk alloy, *Appl. Phys. Lett.* **93**, 193121 (2008).
- [24] Z. Aksamija, Lattice thermal transport in Si-based nanocomposites for thermoelectric applications, *J. Electron. Mater.* **44**, 1644 (2015).
- [25] Z. Zhu, J. Xiao, H. Sun, Y. Hua, R. Cao, Y. Wanga, L. Zhao, and J. Zhuang, Composition-dependent band gaps and indirect-direct band gap transitions of group-IV semiconductor alloys, *Phys. Chem. Chem. Phys.* **17**, 21605 (2015).
- [26] P. Moontragoon, R. A. Soref, and Z. Ikonik, The direct and indirect bandgaps of unstrained $\text{Si}_x\text{Ge}_{1-x-y}\text{Sn}_y$ and their photonic device applications, *J. Appl. Phys.* **112**, 073106 (2012).
- [27] P. I. Gaiduk, J. Lundsgaard Hansen, A. Nylandsted Larsen, F. L. Bregolin, and W. Skorupa, Suppression of tin precipitation in SiSn alloy layers by implanted carbon, *Appl. Phys. Lett.* **104**, 231903 (2014).
- [28] J. Kouvetakis, J. Menendez, and A. V. G. Chizmeshya, Tin-based group IV semiconductors: New platforms for opto- and microelectronic on silicon, *Annu. Rev. Mater. Res.* **36**, 497 (2006).
- [29] R. Soref, J. Kouvetakis, J. Tolle, J. Menendez, and V. D’Costa, Advances in SiGeSn technology, *J. Mater. Res.* **22**, 3281 (2007).
- [30] Inga A. Fischer *et al.*, Growth and characterization of SiGeSn quantum well photodiodes, *Opt. Express* **23**, 25048 (2015).
- [31] K. S. Min and H. A. Atwater, Ultrathin pseudomorphic Sn/Si and $\text{Sn}_x\text{Si}_{1-x}/\text{Si}$ heterostructures, *Appl. Phys. Lett.* **72**, 1884 (1998).
- [32] P. Carruthers, Theory of thermal conductivity of solids at low temperatures, *Rev. Mod. Phys.* **33**, 92 (1961).
- [33] D. T. Morelli, J. P. Heremans, and G. A. Slack, Estimation of the isotope effect on the lattice thermal conductivity of group IV and group III–V semiconductors, *Phys. Rev. B* **66**, 195304 (2002).
- [34] B. Abeles, D. S. Beers, G. D. Cody, and J. P. Dismukes, Thermal conductivity of Ge-Si alloys at high temperatures, *Phys. Rev.* **125**, 44 (1962).
- [35] S. I. Tamura, Isotope scattering of dispersive phonons in Ge, *Phys. Rev. B* **27**, 858 (1983).
- [36] H. J. Maris, Phonon propagation with isotope scattering and spontaneous anharmonic decay, *Phys. Rev. B* **41**, 9736 (1990).
- [37] G. Gilat and L. J. Raubenheimer, Accurate numerical method for calculating frequency-distribution functions in solids, *Phys. Rev.* **144**, 390 (1966).
- [38] W. Liu and M. Asheghi, Thermal conduction in ultrathin pure and doped single-crystal silicon layers at high temperatures, *J. Appl. Phys.* **98**, 123523 (2005).
- [39] M. M. Rieger and P. Vogl, Electronic-band parameters in strained $\text{Si}_{1-x}\text{Ge}_x$ alloys on $\text{Si}_{1-y}\text{Ge}_y$ substrates, *Phys. Rev. B* **48**, 14276 (1993).
- [40] B. Abeles, Lattice thermal conductivity of disordered semiconductor alloys at high temperatures, *Phys. Rev.* **131**, 1906 (1963).
- [41] G. Slack, in *Solid State Physics*, edited by F. Seitz, H. Ehrenreich, and D. Turnbull (Academic, New York, 1979), Vol. 34.
- [42] J. E. Turney, A. J. H. McGaughey, and C. H. Amon, In-plane phonon transport in thin films, *J. Appl. Phys.* **107**, 024317 (2010).
- [43] E. H. Sondheimer, The mean free path of electrons in metals, *Adv. Phys.* **1**, 1 (1952).

- [44] John Cuffe *et al.*, Phonons in slow motion: Dispersion relations in ultrathin Si membranes, *Nano Lett.* **12**, 3569 (2012).
- [45] Y. He, D. Donadio, and G. Galli, Morphology and temperature dependence of the thermal conductivity of nanoporous SiGe, *Nano Lett.* **11**, 3608 (2011).
- [46] Sanghamitra Neogi *et al.*, Tuning thermal transport in ultrathin silicon membranes by surface nanoscale engineering, *ACS Nano* **9**, 3820 (2015).
- [47] J. P. Feser, E. M. Chan, A. Majumdar, R. A. Segalman, and J. J. Urban, Ultralow thermal conductivity in polycrystalline CdSe thin films with controlled grain size, *Nano Lett.* **13**, 2122 (2013).
- [48] P. G. Klemens, *Solid State Physics* (Academic Press, New York, 1958).
- [49] W. Weber, Adiabatic bond charge model for the phonons in diamond, Si, Ge, and α -Sn, *Phys. Rev. B* **15**, 4789 (1977).
- [50] P. Martin, Z. Aksamija, E. Pop, and U. Ravaioli, Impact of Phonon-Surface Roughness Scattering on Thermal Conductivity of Thin Si Nanowires, *Phys. Rev. Lett.* **102**, 125503 (2009).
- [51] K. C. Rustagi and W. Weber, Adiabatic bond charge model for the phonons in $A^3 B^5$ semiconductors, *Solid State Commun.* **18**, 673 (1976).
- [52] D. Strauch and B. Dorner, Phonon dispersion in GaAs, *J. Phys. Condens. Matter* **2**, 1457 (1990).
- [53] B. D. Rajput and D. A. Browne, Lattice dynamics of II–VI materials using the adiabatic bond-charge model, *Phys. Rev. B* **53**, 9052 (1996).
- [54] J. M. Larkin and A. J. H. McGaughey, Predicting alloy vibrational mode properties using lattice dynamics calculations, molecular dynamics simulations, and the virtual crystal approximation, *J. Appl. Phys.* **114**, 023507 (2013).
- [55] Z. Tian, M. Li, Z. Ren, H. Ma, A. Alatas, S. D. Wilson, and J. Li, Inelastic x-ray scattering measurements of phonon dispersion and lifetimes in $PbTe_{1-x}Se_x$ alloys, *J. Phys. Condens. Matter* **27**, 375403 (2015).
- [56] D. L. Price, J. M. Rowe, and R. M. Nicklow, Lattice dynamics of grey tin and indium antimonide, *Phys. Rev. B* **3**, 1268 (1971).
- [57] N. I. Uchida, T. Maeda, R. R. Lieten, S. Okajima, Y. Ohishi, R. Takase, M. Ishimaru, and J. P. Locquet, Carrier and heat transport properties of polycrystalline GeSn films on SiO_2 , *Appl. Phys. Lett.* **107**, 232105 (2015).
- [58] A. Frachioni and B. E. White, Simulated thermal conductivity of silicon-based random multilayer thin films, *J. Appl. Phys.* **112**, 014320 (2012).
- [59] A. A. Tonkikh, N. D. Zakharov, C. Eisenschmidt, H. S. Leipner, and P. Werner, Aperiodic SiSn/Si multilayers for thermoelectric applications, *J. Cryst. Growth* **392**, 49 (2014).
- [60] M. Kurosawa, M. Kato, T. Yamaha, N. Taoka, O. Nakatsuka, and S. Zaima, Near-infrared light absorption by polycrystalline SiSn alloys grown on insulating layers, *Appl. Phys. Lett.* **106**, 171908 (2015).
- [61] J. P. Dismukes, L. Ekstrom, E. F. Steigmeier, I. Kudman, and D. S. Beers, Thermal and electrical properties of heavily doped Ge-Si alloys up to 1300°K, *J. Appl. Phys.* **35**, 2899 (1964).
- [62] D. G. Cahill, S. K. Watson, and R. O. Pohl, Lower limit to the thermal conductivity of disordered crystals, *Phys. Rev. B* **46**, 6131 (1992).
- [63] Bed Poudel *et al.*, High-thermoelectric performance of nanostructured bismuth antimony telluride bulk alloys, *Science* **320**, 634 (2008).
- [64] Y. Lan, A. J. Minnich, G. Chen, and Z. Ren, Enhancement of thermoelectric figure-of-merit by a bulk nanostructuring approach, *Adv. Funct. Mater.* **20**, 357 (2010).
- [65] M. V. Fischetti and S. E. Laux, Band structure, deformation potentials, and carrier mobility in strained Si, Ge, and SiGe alloys, *J. Appl. Phys.* **80**, 2234 (1996).
- [66] G. H. Zhu *et al.*, Increased Phonon Scattering by Nanograins and Point Defects in Nanostructured Silicon with a Low Concentration of Germanium, *Phys. Rev. Lett.* **102**, 196803 (2009).
- [67] A. M. Hussain, N. Singh, H. Fahad, K. Rader, U. Schwingenschlögl, and M. Hussain, Exploring SiSn as a performance enhancing semiconductor: A theoretical and experimental approach, *J. Appl. Phys.* **116**, 224506 (2014).
- [68] K. W. Adu, H. R. Gutierrez, U. J. Kim, G. U. Sumanasekera, and P. C. Eklund, Scaling laws of cumulative thermal conductivity for short and long phonon mean free paths, *Appl. Phys. Lett.* **105**, 131901 (2014).
- [69] M. Bauer, C. Ritter, P. A. Crozier, J. Ren, J. Menendez, G. Wolf, and J. Kouvetakis, Synthesis of ternary SiGeSn semiconductors on Si(100) via Sn_xGe_{1-x} buffer layers, *Appl. Phys. Lett.* **83**, 2163 (2003).
- [70] V. R. D'Costa, Y.-Y. Fang, J. Tolle, J. Kouvetakis, and J. Menéndez, Tunable Optical Gap at a Fixed Lattice Constant in Group-IV Semiconductor Alloys, *Phys. Rev. Lett.* **102**, 107403 (2009).
- [71] J. D. Sau and M. L. Cohen, Possibility of increased mobility in Ge-Sn alloy system, *Phys. Rev. B* **75**, 045208 (2007).
- [72] J. O. Sofo and G. D. Mahan, Optimum band gap of a thermoelectric material, *Phys. Rev. B* **49**, 4565 (1994).
- [73] I. Bejenari and V. Kantser, Thermoelectric properties of bismuth telluride nanowires in the constant relaxation-time approximation, *Phys. Rev. B* **78**, 115322 (2008).
- [74] L. M. Goncalves, C. Couto, P. Alpuim, A. G. Rolo, F. Völklein, and J. H. Correia, Optimization of thermoelectric properties on Bi_2Te_3 thin films deposited by thermal co-evaporation, *Thin Solid Films* **518**, 2816 (2010).